Metal to non-metal sites of metallic sulfides switching products from CO to CH_4 for photocatalytic CO_2 reduction

Yao Chai[1,4], Yuehua Kong [2,4], Min Lin[1], Wei Lin [2], Jinni Shen[1], Jinlin Long [1], Rusheng Yuan[1], Wenxin Dai [1,3], Xuxu Wang [1] & Zizhong Zhang [1,3] ✉

The active center for the adsorption and activation of carbon dioxide plays a vital role in the conversion and product selectivity of photocatalytic CO_2 reduction. Here, we find multiple metal sulfides $CuInSnS_4$ octahedral nanocrystal with exposed (1 1 1) plane for the selectively photocatalytic CO_2 reduction to methane. Still, the product is switched to carbon monoxide on the corresponding individual metal sulfides In_2S_3, SnS_2, and Cu_2S. Unlike the common metal or defects as active sites, the non-metal sulfur atom in $CuInSnS_4$ is revealed to be the adsorption center for responding to the selectivity of CH_4 products. The carbon atom of CO_2 adsorbed on the electron-poor sulfur atom of $CuInSnS_4$ is favorable for stabilizing the intermediates and thus promotes the conversion of CO_2 to CH_4. Both the activity and selectivity of CH_4 products over the pristine $CuInSnS_4$ nanocrystal can be further improved by the modification of with various co-catalysts to enhance the separation of the photogenerated charge carrier. This work provides a non-metal active site to determine the conversion and selectivity of photocatalytic CO_2 reduction.

The solar-energy-driven photocatalytic conversion of CO_2 with H_2O into hydrocarbon fuels is a significant solution for simultaneously addressing global energy demands and climate change issues[1-4]. Various products of CO_2 reduction from photocatalytic multi-electron processes, including CO (two electrons), HCOOH (two electrons), HCHO (four electrons), CH_3OH (six electrons), and CH_4 (eight electrons), have been produced by a great variety of photocatalysts[5-8]. Achieving both high selectivity and high conversion for photocatalytic CO_2 reduction is highly desirable in the field of photocatalysis research. However, efficient photoreduction of CO_2 is very challenging, both in terms of chemical thermodynamics and kinetics, due to the highly stable structure of CO_2 and the involvement of multiple proton-coupled electron transfer[9-11]. Additionally, the regulation of product selectivity in photocatalytic CO_2 conversion remains an unknown challenge.

It has been well understood for the photocatalytic process that the identification of the active centers of catalysts for the adsorption and activation of CO_2 is prerequisite for efficient CO_2 conversion and product selectivity. Constructing an active center of catalysts for the adsorption and activation of CO_2 is an efficient solution to improve CO_2 conversion efficiency and product selectivity[12-14]. Various metal-free photocatalysts were reported for CO_2 reduction[15-19], typically such as covalent organic frameworks, graphitic carbon nitride, elemental phosphorus, boron nitride, and silicon carbide[20-24]. These metal-free photocatalysts have non-metallic sites as the adsorption and activation sites of CO_2 molecules and thus photocatalytical CO_2 reduction[20,25-28]. However, for metal oxide or sulfide photocatalysts, many studies suggest that metal components or defects on photocatalysts play a crucial role as primary sites in the adsorption and activation of CO_2 and thus affect product selectivity[29]. Zhou et al. reported that the S vacancy

[1]State Key Lab of Photocatalysis on Energy and Environment, College of Chemistry, Fuzhou University, Fuzhou, P. R. China. [2]College of Chemistry, Fuzhou University, Fuzhou, P. R. China. [3]Qingyuan Innovation Laboratory, Quanzhou, P. R. China. [4]These authors contributed equally: Yao Chai, Yuehua Kong. ✉e-mail: z.zhang@fzu.edu.cn

or Cd vacancy CdS with single Au atom deposition for CO_2 adsorption is different[30]. CO_2 prefers to physically adsorb on single Au atoms of Au/CdS_{1-x} and photoreduction into CO, while CO_2 is more likely to chemically bond on the Cd vacancies of $Au/Cd_{1-x}S$, resulting in a remarkable CO and CH_4 generation rate on $Au/Cd_{1-x}S$. He et al. synthesized a $ZnIn_2S_4$ nanosheet photocatalyst with abundant Zn vacancies[31], where CO_2 can be efficiently adsorbed on Zn vacancies to form CO_2^- species and highly selective photoreduction into CO. Yu et al. designed a Cu_3SnS_4 photocatalyst with S vacancies to increase ratios of Cu (I/II) for CO_2 photoreduction[32]. The formed Cu (I) acts as adsorption sites for CO_2, conducive to further hydrogenation of CO intermediate into CH_4. Xie et al. showed that the defect-state $CuIn_5S_8$ ultrathin nanosheets have low-coordination Cu and In sites for CO_2 adsorption to form highly stable Cu-C-O-In intermediates, which tend to obtain 100% CH_4 selectivity[33]. Xu et al. designed a Co-Ni-P NH/BP catalyst with bimetallic sites to form a highly stable Co-O-C-Ni intermediate for the selective photoreduction of CO_2 to CH_4[34]. However, the complex structures of defects on photocatalyst make it only a plausible correlation between defect structures and product selectivity. Some research shows that the adsorbed interaction between CO_2 and metal sites is relatively weak since the formed metal-C bonds are weaker than the highly stable C=O bonds in CO_2. This leads to the easy cleaving of metal-C bonds during the reaction process, hindering the deep reduction of CO_2 into hydrocarbons[30]. Obviously, the non-metal sites on metal sulfide photocatalysts are very rarely considered the primary active center for the adsorption and activation of CO_2.

Here, we have successfully prepared multiple metal sulfides, including $CuInSnS_4$ octahedral nanocrystal and corresponding individual metal sulfides In_2S_3, SnS_2, and Cu_2S, through a simple one-step hydrothermal method. The $CuInSnS_4$ nanocrystal is thermodynamically favorable to activate CO_2 and leads to a switch of main products from CO to CH_4 with a yield of 6.53 μL h⁻¹ for the visible-light-driven CO_2

reduction with H_2O vapor without the assistance of any noble metal cocatalysts. In contrast, individual metal sulfides can only produce CO. We reveal that different adsorption configurations of CO_2 on metal sulfides lead to different products in CO_2 photoreduction. The non-metal sulfur atom in the prepared multiple metal sulfides $CuInSnS_4$ octahedron nanocrystal is thermodynamically favorable to activate CO_2 and leads to a switch of main products to CH_4, as compared with the common individual metal sulfides In_2S_3, SnS_2 and Cu_2S with metal center as active sites to form CO products. CO_2 is revealed to be adsorbed on the S atom center of $CuInSnS_4$ to form an S-C-O-In structural unit, which is more conducive to protonation and leads to the efficient photocatalytic yield of CH_4. Thus, we provide an insight into the role of non-metal center of photocatalyst in determining the conversion and selectivity of photocatalytic CO_2 reduction. Although the pristine $CuInSnS_4$ only exhibits a yield of CH_4 evolution of 6.53 μL h⁻¹ (corresponding to 5.83 μmol h⁻¹ g⁻¹), the activity and selectivity of CH_4 evolution on $CuInSnS_4$ can be significantly improved by modifying with cocatalysts such as Pt, CoO, NiO, and $Co(OH)_2$. We believe that this knowledge can contribute to the development of more efficient and selective photocatalysts for CO_2 reduction in the future.

Results
Characterization of $CuInSnS_4$ octahedral nanocrystal
The as-prepared $CuInSnS_4$ nanocrystals belong to the cubic spinel structure (JCPDS No. 29-0548), as revealed by the X-ray diffraction pattern (Fig. 1a), which were prepared through a simple one-step hydrothermal reaction. The hydrothermal temperature (160 °C, 180 °C, and 200 °C) did not have any evident impact on the crystalline and purity of $CuInSnS_4$ (Supplementary Fig. 1). Under similar hydrothermal processes, In_2S_3 with a tetragonal crystal phase structure (JCPDS No. 25-0390), SnS_2 with a hexagonal crystal phase (JCPDS No. 23-0677), and Cu_2S with a cubic crystal phase were also prepared (JCPDS No. 02-1284)
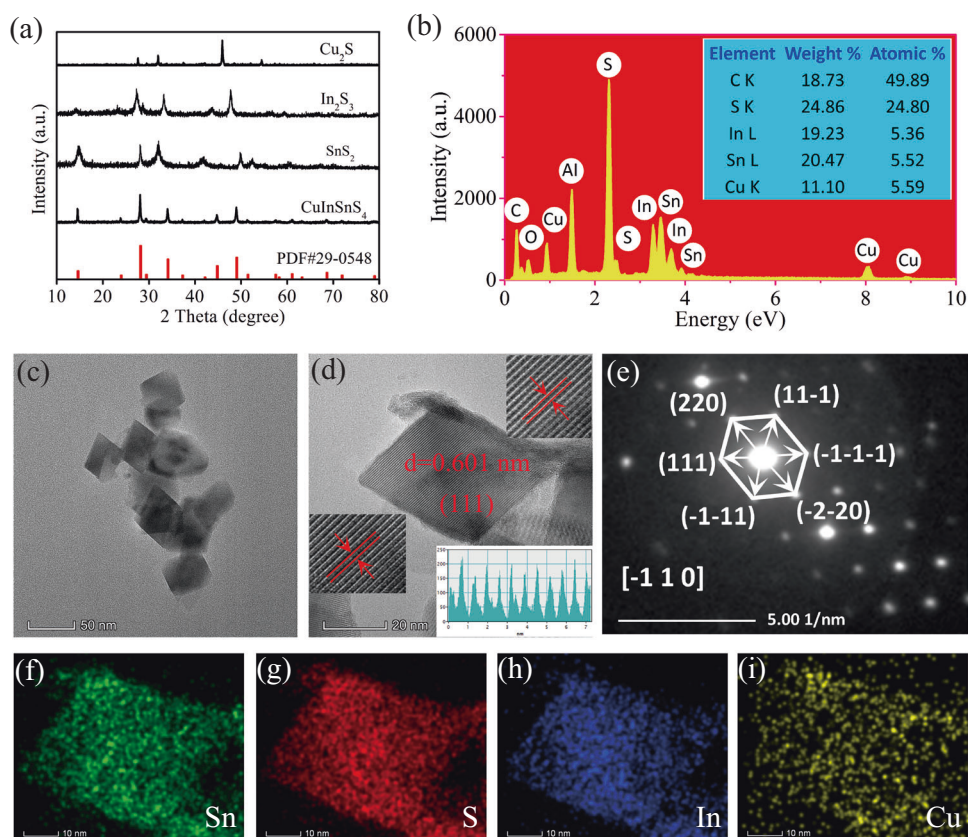

Fig. 1 | The characterization of crystal phase, composition, and morphology. a XRD patterns of several metal sulfides, **b** EDS spectra of $CuInSnS_4$ photocatalyst, **c** a TEM image of $CuInSnS_4$ sample, **d** an HRTEM image, and **e** an SAED pattern of the $CuInSnS_4$ sample, as well as **f–i** EDS elemental mapping images.

(Supplementary Fig. 2). The cubic spinel $CuInSnS_4$ crystal structure shows that either In or Sn atom is coordinated with six S atoms to form an octahedron structure, while Cu atom is formed by a $[CuS_4]$ tetrahedral structural unit (Supplementary Fig. 3). For comparison, in In_2S_3 crystals, the In atom is present in $[InS_4]$ tetrahedron and $[InS_6]$ octahedron coordination (Supplementary Fig. 4). Cu and Sn atoms exist as $[CuS_4]$ tetrahedron and $[SnS_6]$ octahedron coordination in Cu_2S and SnS_2 crystal structure, respectively (Supplementary Figs. 5, 6). The coordination structure of each metal in $CuInSnS_4$ coincides with the individual Cu_2S, In_2S_3, and SnS_2. The composition of $CuInSnS_4$ is analyzed by energy-dispersive spectroscopy, as shown in Fig. 1b. EDS offers that the Cu, Sn, In, and S atomic ratio is ~1:1:1:4, very close to the stoichiometric value of $CuInSnS_4$ compounds, indicating the high purity of $CuInSnS_4$ nanocrystal. Meantime, the ICP-MS test results of the metal element content of the nano-single crystal $CuInSnS_4$ sample are presented in Table S1. The atomic ratio of Cu:In:Sn is 1.06:1.00:1.00, which closely matches the theoretical value of $CuInSnS_4$. Supplementary Fig. 7 shows the SEM images of In_2S_3, Cu_2S, and SnS_2 samples. In_2S_3 exhibits a morphology of microspheres self-assembled from nanosheets. Cu_2S has the basic shape of nanoparticles, while SnS_2 displays the morphology of ultrathin nanosheets. Both scanning electron microscopy and transmission electron microscopy images of nanoscale microstructure confirm that the prepared $CuInSnS_4$ displays an octahedral nanocrystal structure with a size of about 30 nm (Supplementary Fig. 8 and Fig. 1c). The high-resolution TEM image (Fig. 1d) shows the exposed facets of the octahedron with a lattice spacing of 0.601 nm, which is assigned to (111) facets of $CuInSnS_4$. Selected area electron diffraction further verifies that the $CuInSnS_4$ sample not only exposes the (1 1 1) crystal plane but also has a single crystal structure (Fig. 1e). All the results confirm the successful preparation of $CuInSnS_4$ nanocrystal with high-quality exposed (1 1 1) crystal faces. The specific surface area of the $CuInSnS_4$ sample is about 24.1 $m^2 g^{-1}$, while that of the prepared In_2S_3, SnS_2, and Cu_2S are 26.8 $m^2 g^{-1}$, 37.6 $m^2 g^{-1}$, and 3.6 $m^2 g^{-1}$, respectively (Supplementary Fig. 9). As displayed in Fig. 1f−i, the uniform distribution of Sn, S, In, and Cu elements in $CuInSnS_4$ octahedral nanoparticles indicates that the catalyst is of high purity.

X-ray photoelectron spectroscopy was used to compare the electronic states of the obtained sample. The $Cu2p_{3/2}$ and $Cu2p_{1/2}$ binding energies of $CuInSnS_4$ sample are 932.07 eV and 951.90 eV, respectively (Fig. 2a). This demonstrates that the valence state of Cu is +1 in the $CuInSnS_4$ sample[35,36], which is also confirmed by the Cu LMM spectra (Supplementary Fig. 10). Notably, the $Cu2p$-binding energies of the $CuInSnS_4$ sample is identical to that of Cu_2S. The binding energies of $In3d_{5/2}$ and $In3d_{3/2}$ in the $CuInSnS_4$ sample are 444.63 eV and 452.18 eV, respectively. These values indicate that the valence state of In in the $CuInSnS_4$ sample is +3. Compared with In_2S_3, the $In3d$ binding energy of $CuInSnS_4$ uniformly shifts toward the lower binding energy, as shown in Fig. 2b. This is attributed to the difference in the In coordinated environment between $CuInSnS_4$ and In_2S_3 because the partial In atom in In_2S_3 exists in the state of $[InS_4]$ tetrahedron[37]. In the $CuInSnS_4$ sample, the $Sn3d_{5/2}$ and $Sn3d_{3/2}$ doublets are centered respectively at 486.30 eV and 494.70 eV, assigning to Sn^{4+} valence state. Notably, the binding energy of Sn in $CuInSnS_4$ is slightly lower than that in the parent SnS_2 (Fig. 2c). The possible reason is that the Sn atoms are in different crystal structures[38]. Furthermore, the binding energies of $S2p_{3/2}$ and $S2p_{1/2}$ in the $CuInSnS_4$ sample are measured to be 161.45 eV and 162.70 eV, respectively, which corresponds to the S^{2-} valence state. In the $S2p$ XPS spectra, the binding energies of S atoms increase in the order of $Cu_2S < In_2S_3 < SnS_2 < CuInSnS_4$, as shown in Fig. 2d. S atoms in $CuInSnS_4$ have the highest binding energy. This is interpreted by the fact that the average bond length (0.253 nm) between sulfur and metal atoms in $CuInSnS_4$ is slightly larger than in monometallic sulfide[4,37,39]. Moreover, the S atom in $CuInSnS_4$ has a higher binding energy than that of monometallic sulfides, indicating an electron-deficient state of the S atoms in $CuInSnS_4$ compared to monometallic sulfides. This electron-deficient state of the S atom in $CuInSnS_4$ can serve as the reaction site for CO_2 adsorption and activation.

Photocatalytic conversion of CO_2 and H_2O vapor

The photocatalytic CO_2 reduction performance of the samples was evaluated in a customized sealed quartz glass vessel, in a gas-solid reaction system, with a small amount of water vapor in a CO_2
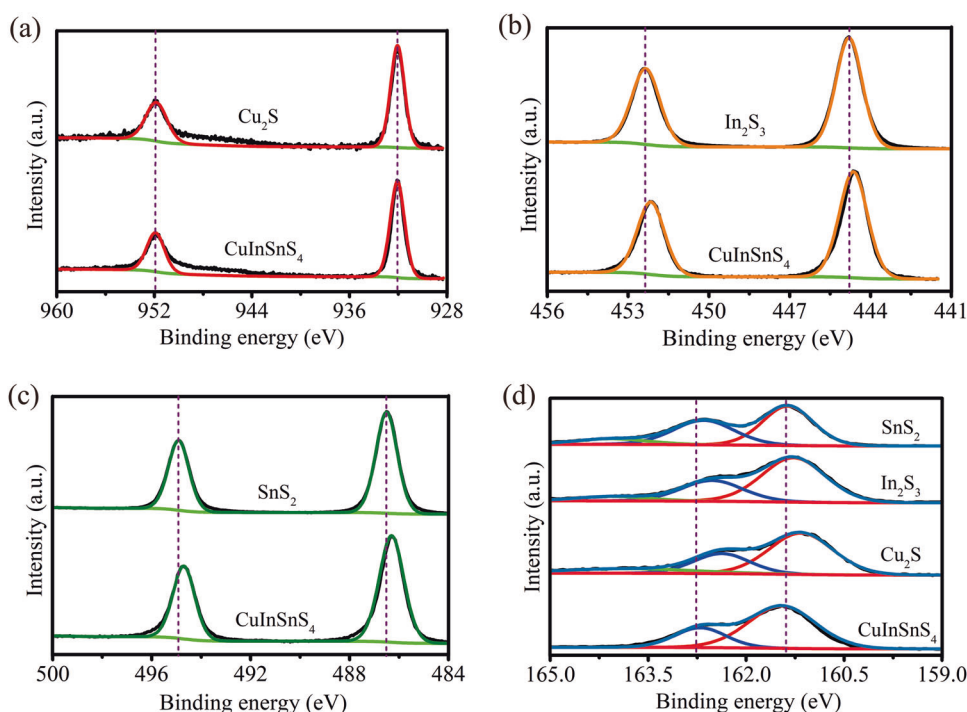

Fig. 2 | Characterization of electronic structure. High-resolution XPS spectra of metal sulfides: **a** $Cu2p$, **b** $In3d$, **c** $Sn3d$, and **d** $S2p$.

atmosphere, under the irradiation of a 300 W Xe lamp with a 420 nm cutoff wavelength filter (Supplementary Fig. 11). It is important to note that this reaction is a gas-solid phase reaction. The system contains only 50 μL of water, which evaporates into water vapor upon injection into the reactor. As a result, only gaseous products such as CH_4, CO, and a small amount of H_2 are detected, while liquid products (such as CH_3OH, HCHO, HCOOH, etc.) are not detected. Figure 3a shows the corresponding photocatalytic CO_2 performance of the samples under visible-light irradiation. For single metal sulfides In_2S_3, Cu_2S, and SnS_2, CO is the main product with a yield rate of less than 3.2 μL h^{-1} from photocatalytic CO_2 reduction, while the multi-electron transfer product CH_4 is hardly formed. Whereas, the $CuInSnS_4$ sample shows excellent photocatalytic CO_2 reduction performance, yielding CH_4 as the main product besides a slight amount of CO and H_2 evolution. The hydrothermal temperature has no obvious impact on the CO_2 reduction performance of $CuInSnS_4$ (Supplementary Fig. 12). The rate of CH_4 generation reaches 6.53 μL h^{-1} for the $CuInSnS_4$ sample. The selectivity of CH_4 is calculated to be 67.3% based on the contents of carbon-containing products. The significant difference in the product selectivity demonstrates the different mechanisms of CO_2 reduction or the different active sites between $CuInSnS_4$ and single metal sulfides. The controlled blank experiments under other conditions were investigated to confirm the occurrence of CO_2 reduction on $CuInSnS_4$, as shown in Supplementary Fig. 13. The CH_4 product is not detected without either light irradiation or catalyst, proving that CO_2 reduction is a light-induced catalytic reaction on $CuInSnS_4$. Meanwhile, without adding H_2O into the reaction system, only a very few products are detected, indicating that H_2O is also one of the essential reactants involved in the reaction. When N_2 is used instead of CO_2 for the reaction, only a small amount of CO is detected, directly proving that the source of CO and CH_4 products is CO_2. The presence of small amounts of CO may be attributed to contamination from ambient air, reactors, and equipment, as we can see that small CO products is also

detected without $CuInSnS_4$ photocatalysts[40]. Figure 3b shows the stability of the $CuInSnS_4$ sample for photocatalytic reduction of CO_2. It is clear that the $CuInSnS_4$ sample presents good performance without noticeable activity decrement after three-cycle photocatalytic CO_2 reduction tests of a total of 27 h (9 h visible-light irradiation for each cycle). Neither crystal structural transformation nor absorption behavior changes are found in the XRD pattern and ultraviolet–visible diffuse reflectance spectra for the $CuInSnS_4$ sample after photocatalytic reaction (Supplementary Fig. 14). These results suggest that $CuInSnS_4$ possesses good stability during photocatalytic CO_2 reduction. Moreover, the XPS of the catalyst after the reaction shows that a weak photocorrosion phenomenon occurs in $CuInSnS_4$[41,42] (Supplementary Fig. 15). Specifically, the photogenerated holes or the active oxygen species oxidize the surface S^{2-} of the catalyst to SO_3^{2-}. The peaks with binding energies in the range of 168.26-170.26 eV are assigned to the XPS peaks of SO_3^{2-} species (Supplementary Fig. 16). The photocatalytic performance of $CuInSnS_4$ sample is evaluated under different monochromatic light wavelengths in Fig. 3c. It is observed that as the wavelength of the incident light increases, the photocatalytic activity significantly decreases. However, the $CuInSnS_4$ nano-single crystal photocatalyst demonstrates a CH_4 generation rate of 0.69 μL h^{-1} and CO generation rate of 0.22 μL h^{-1} under the irradiation of 525 nm monochromatic light, which is surprising. The different monochromatic light tests indicate that $CuInSnS_4$ is an exceptional catalyst for CO_2 photoreduction under visible light. The $^{13}CO_2$ isotope experiment further validates that CH_4 product is generated from the photoreduction of CO_2 molecules, where only $^{13}CH_4$ is detected when the reaction is carried out in a $^{13}CO_2$ atmosphere, as shown in Fig. 3d. Meanwhile, the $^{13}CO_2$ isotope also confirms that the generated CO was indeed a product of CO_2 photoreduction. When the reaction is conducted in a $^{13}CO_2$ atmosphere, the weak peak of ^{13}CO with a m/z = 29 was detected due to the low activity of $CuInSnS_4$ for CO evolution (Supplementary Fig. 17a). It is noteworthy that the mass spectrum peak
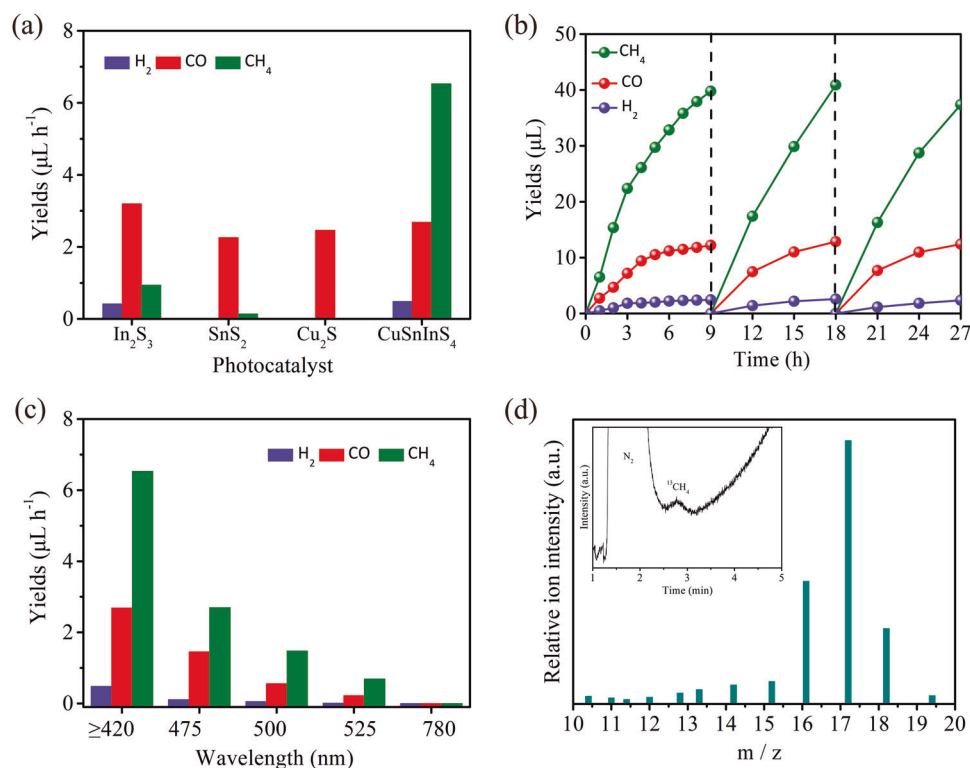

Fig. 3 | Photocatalytic conversion performance of CO_2 and H_2O. a The production rate of CH_4, CO, and H_2 in various photocatalysts under visible-light conditions. **b** Photocatalytic CO_2 reduction stability test of $CuInSnS_4$ sample. **c** Photocatalytic performance of $CuInSnS_4$ sample under monochromatic light irradiation. **d** GC-MS spectra of $^{13}CH_4$ generated from $^{13}CO_2$.

at m/z = 28 corresponds to the N_2 molecule from air interference, as evident from the distinct N_2 peaks in chromatogram. Additionally, the $^{12}CO_2$ experiment further evidences that the generated CO results from the photoreduction of CO_2 molecules with no peaks at m/z = 29 (Supplementary Fig. 17b).

Although the pristine $CuInSnS_4$ only exhibits a yield of CH_4 evolution of 6.53 μL h^{-1} (corresponding to 5.83 μmol h^{-1} g^{-1}) with a selectivity of 67.3%, the activity and selectivity of CH_4 evolution on $CuInSnS_4$ can be improved by coupling with semiconductor photocatalysts or noble metals as cocatalysts. We evaluated the photocatalytic performance of $CuInSnS_4$ modified with Pt, CoO, NiO, $Co(OH)_2$, and dual co-catalysts Pt and $Co(OH)_2$, for the CO_2 reduction reaction. The composition and chemical states of Pt, CoO, NiO, $Co(OH)_2$ cocatalysts are well verified by XRD patterns and XPS spectra (Supplementary Figs. 18–23). Table S2 lists a comparison of the photoreduction activity of $CuInSnS_4$ and co-catalyst-modified $CuInSnS_4$ photocatalysts, along with the common metal sulfide systems currently used for CO_2 photoreduction. Clearly, both the yield and selectivity of CH_4 evolution on $CuInSnS_4$ can be significantly improved by modifying with cocatalysts such as Pt, CoO, NiO, and $Co(OH)_2$. The activity of CH_4 evolution on the modified $CuInSnS_4$ photocatalysts surpasses the majority of the reported photocatalysts for CO_2 reduction up to now. Particularly, the incorporation of $Co(OH)_2$ as a cocatalyst significantly enhances the CO_2 photoreduction activity of the $CuInSnS_4$ photocatalyst. As the $Co(OH)_2$ loading increases, the photoreduction activity of CO_2 exhibits a characteristic volcanic pattern. With 5%$Co(OH)_2$ loading onto $CuInSnS_4$, the production rates for CH_4 and CO, respectively, reach 145.45 and 32.32 μmol h^{-1} g^{-1}, corresponding to a CH_4 selectivity of 81.8%. The generation rates of CH_4 and CO are 25 times and 13 times that of pure $CuInSnS_4$, respectively. Furthermore, when $CuInSnS_4$ is modified with a dual co-catalyst of 5% $Co(OH)_2$ as an oxidation co-catalyst and 1%Pt as a reduction co-catalyst, CH_4 production reaches 195.60 μmol h^{-1} g^{-1}, along with 22.00 μmol h^{-1} g^{-1} of CO, and a CH_4 selectivity of 89.9%. Photoelectrochemical characterization was employed to assess the separation efficiency of photogenerated carriers on the modified $CuInSnS_4$, as shown in Supplementary Fig. 24. Clearly, the $CuInSnS_4$ samples modified with the co-catalyst exhibit a higher photocurrent signal and a smaller electrochemical impedance radius as compared to the parent $CuInSnS_4$ sample. The photocurrent increases sequentially in the order of $CuInSnS_4$ < 5%$Co(OH)_2$/$CuInSnS_4$ ≈ 1%Pt/$CuInSnS_4$ < 5%$Co(OH)_2$/$CuInSnS_4$/1%Pt, indicating that the modification of the dual co-catalyst improves photoelectric carrier separation and migration compared to the single co-catalyst. The NiO and CoO cocatalysts also improve the separation efficiency and migration rate of the photogenerated carriers of $CuInSnS_4$ photocatalyst. The decreasing order of electrochemical resistance radius is $CuInSnS_4$ > 1%Pt/$CuInSnS_4$ ≈ 5%$Co(OH)_2$/$CuInSnS_4$ > 5%$Co(OH)_2$/$CuInSnS_4$/1%Pt, consistent with the photocatalytic activity trend. Additionally, both 10%NiO/$CuInSnS_4$ and 10% CoO/$CuInSnS_4$ exhibit smaller electrochemical resistance radii than pure $CuInSnS_4$, confirming that the cocatalyst promotes the photogenerated charge separation and migration. Therefore, the modification of $CuInSnS_4$ with various cocatalysts to enhance the separation of photogenerated carriers is related to the activity and selectivity of CH_4 products. The apparent quantum yield is calculated by measuring the yield of CH_4 and CO in 5%$Co(OH)_2$/$CuInSnS_4$/1%Pt under monochromatic light at 400 nm. Supplementary Fig. 25 shows the spectrum and intensity of monochromatic light at 400 nm. Under 400 nm monochromatic light irradiation, the apparent quantum efficiencies for CH_4 and CO are 0.16% and 0.01%, respectively. Based on the above analysis, we believe that $CuInSnS_4$ nano-single crystal photocatalysts through further optimization design of the different contents and types of cocatalyst modification can be more efficient and selective for CO_2 reduction in the future.

Energy band and photoelectrochemical characterization

The band energy potential is a key determinant of the driving force of redox reactions. Therefore, we have studied the band structure of the catalyst through UV-vis DRS and XPS valence band spectroscopy. As shown in Fig. 4a and Supplementary Fig. 26, the optical absorption band edge of $CuInSnS_4$ is calculated to be 787.5 nm, which corresponds to a band gap energy of 1.57 eV. For comparison, the absorption band edges of single metal sulfide Cu_2S, SnS_2, and In_2S_3 are 747.0 nm, 552.7 nm, and 641.6 nm, corresponding to the band gap of 1.66 eV, 2.24 eV, and 1.93 eV, respectively. Moreover, the valence band potential of $CuInSnS_4$ is determined to be 0.50 V from the valence band XPS spectra (Supplementary Fig. 27), while the Cu_2S, SnS_2, and In_2S_3 possess valence band potentials of 1.02 V, 1.70 V, and 1.93 V, respectively. By using the formula $E_{CB} = E_g - E_{VB}$, we have determined that the conduction band potentials of $CuInSnS_4$, Cu_2S, SnS_2, and In_2S_3 are −1.15 V, −1.10 V, −0.54 V, and −0.55 V, respectively. Based on the optical band gaps, we have obtained the electronic band energies relative to a normal hydrogen electrode (Fig. 4b), indicating that both $CuInSnS_4$ and single metal sulfides have the ability to reduce CO_2 to CH_4 and CO. Notably, $CuInSnS_4$ exhibits the highest reduction potential for the photogenerated electrons to reduce CO_2. Additionally, $CuInSnS_4$ shows a significantly increased photocurrent density (0.014 mA cm^{-2}) compared to the single metal sulfide under visible-light irradiation (Fig. 4c), indicating a more efficient separation of the photoinduced charge in multi-metal sulfides. The lower interface resistance in the corresponding electrochemical impedance spectra (Fig. 4d) confirms the rapid transfer of photogenerated electrons in $CuInSnS_4$. The efficient separation efficiency and migration rate of photogenerated carriers make polymetallic sulfides exhibit higher photocatalytic CO_2 reduction performance compared to monometallic sulfides. However, the higher migration and separation efficiency of charge carriers in $CuInSnS_4$ alone is not sufficient to explain the substantial difference in the product selectivity between $CuInSnS_4$ and single metal sulfides.

The in situ CO_2 adsorption FT-IR spectra and mechanism

To understand the CO_2 reduction process over $CuInSnS_4$ and single metal sulfides, in situ Fourier-transform infrared spectroscopy is used to compare the reaction intermediates on the catalyst surface. No macroscopic infrared absorption peaks for intermediates are found on Cu_2S or SnS_2, even under light irradiation, possibly due to their weak chemical interaction with CO_2 (Supplementary Fig. 28a, b). However, In_2S_3 shows a significant activation effect on the CO_2 adsorbed on the surface under light irradiation (Fig. 5a). Notably, CO_2 can form chemical adsorption with In_2S_3 even under dark conditions, as indicated by the infrared peak at 1150 cm^{-1}, which can be considered an O-S stretching vibration[43], suggesting that the oxygen atom of CO_2 is bonded to the sulfur atom of In_2S_3. Upon light irradiation, some infrared peaks of the produced intermediates on the catalyst surface are observed. The infrared peak at 1225 cm^{-1} is attributed to the vibration of bidentate bicarbonate[44], while the infrared peak at 1412 cm^{-1} is attributed to the vibration of monodentate bicarbonate[45]. Most importantly, the infrared peak at 1610 cm^{-1} is attributed to the *COOH group, which is generally regarded as the crucial intermediate for CO_2 reduction to CO[46]. Surprisingly, the polymetallic sulfide $CuInSnS_4$ exhibits strong chemisorption of CO_2 and strong physisorption of H_2O (Fig. 5b). The prominent infrared peak observed at 1627 cm^{-1} is attributed to the physical adsorption of H_2O. However, In_2S_3 does not exhibit a noticeable infrared adsorption peak of H_2O at 1627 cm^{-1}. This is because In_2S_3 has a lower affinity towards water adsorption than $CuInSnS_4$, as indicated by the high contact angle on In_2S_3 surface (Supplementary Fig. 29). Moreover, a prominent infrared peak at 1117 cm^{-1} assigned to C-S stretching vibration is observed upon the CO_2 adsorption on $CuInSnS_4$[47–49]. The CO_2 adsorption and
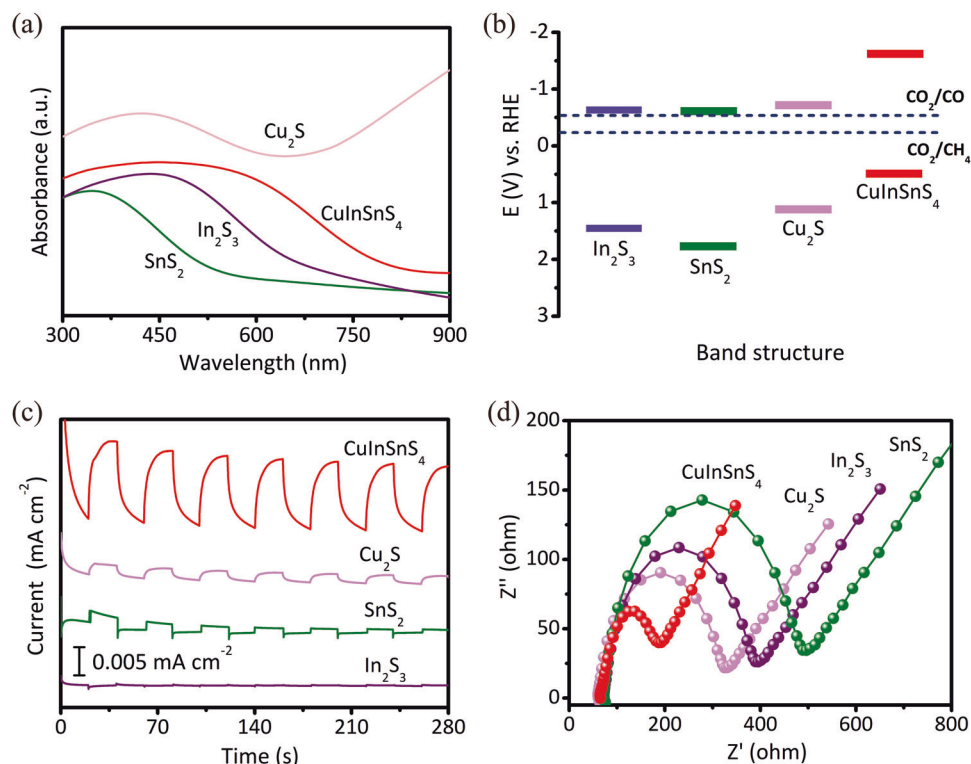
Fig. 4 | Characterization of energy bands and optoelectronic properties. a UV-vis absorption spectrum of various metal sulfides. **b** The optical band gap energy (E_g) of the corresponding CuInSnS$_4$ and various single metal sulfides. **c** Photocurrent response and **d** electrochemical impedance spectroscopy of the as-prepared samples.
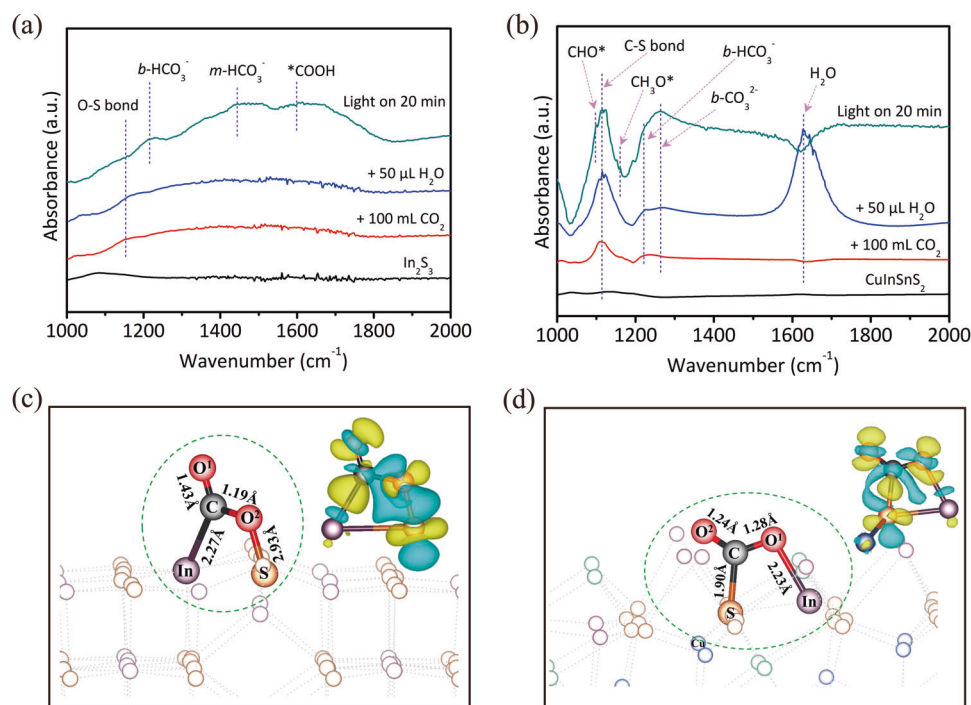

Fig. 5 | In situ CO$_2$ adsorption FT-IR spectra and differential charge density map as well as free energy diagrams of CO$_2$ photoreduction to CH$_4$. In situ FT-IR spectra of CO$_2$ adsorbed on **a** In$_2$S$_3$ and **b** CuInSnS$_4$. CO$_2$ adsorption configuration and differential charge density map of **c** In$_2$S$_3$ and **d** CuSnInS$_4$ photocatalysts. In the differential charge density map, the yellow and blue regions indicate electron accumulation and depletion, respectively.

activation are significantly improved on $CuInSnS_4$ compared to In_2S_3. Furthermore, the adsorption state of CO_2 on $CuInSnS_4$ is different from that on In_2S_3, as the carbon atom of CO_2 is bonded to the sulfur atom of $CuInSnS_4$. Under light conditions, $CuInSnS_4$ produces specific CO_2-activated intermediates, as indicated by the infrared peaks at 1225 cm^{-1} and 1260 cm^{-1}, attributed to the vibration of bidentate bicarbonate and bidentate carbonate[50,51], respectively. Additionally, the infrared peaks at 1100 cm^{-1} and 1160 cm^{-1} are attributed to the absorption peaks of *CHO and *CH_3O, which are intermediates for the yield of CH_4[52,53]. Therefore, either the CO_2 adsorption state in darkness or the produced intermediates under light irradiation show that the sites for CO_2 adsorption and the CO_2 reduction approach differ between single-metal sulfide In_2S_3 and multi-metal sulfide $CuInSnS_4$. This may account for the different selectivity of products between In_2S_3 and $CuInSnS_4$.

It has been demonstrated that sulfur defect sites in multiple metal sulfides acted as an active center for the selective photoreduction of CO_2 to CH_4. However, $CuInSnS_4$ nano-single crystal shows no significant sulfur defect signals compared to the strong defect signals in SnS_2 and In_2S_3, as shown in Supplementary Fig. 30. This indicates that the selectivity of CH_4 products on $CuInSnS_4$ is not related to sulfur defects. The mechanism of selective photocatalytic CO_2 reduction on $CuInSnS_4$ and In_2S_3 photocatalysts is further theoretically studied. Firstly, we investigated the adsorption behavior of CO_2 on the surfaces of In_2S_3 and $CuInSnS_4$. The (0 0 1) crystal plane of the In_2S_3 sample and the (1 1 1) crystal plane of the $CuInSnS_4$ sample were selected as models, and all atoms on the crystal planes were considered as potential sites for CO_2 adsorption activation (Supplementary Figs. 31 and 32). Based on CO_2 adsorption energy, the optimal adsorption models of CO_2 on In_2S_3 and $CuInSnS_4$ photocatalyst surfaces are optimized (Supplementary Figs. 33 and 34). Figure 5c, d depict schematic diagrams of CO_2 stable adsorption configurations and the charge density difference of CO_2 on In_2S_3 and $CuInSnS_4$, respectively. The stable CO_2 adsorption configuration on In_2S_3 is the C atom of CO_2 bonded to In atom with a bond length of 2.27 Å, while the O atom of the CO_2 molecule is bonded with the S atom with a bond length of 1.70 Å. The CO_2 adsorption model for the polymetallic sulfide $CuInSnS_4$ is the opposite. The unique C-S bond with a bond length of 1.90 Å is formed between the C atom of CO_2 and the surface S atom, and one O atom of

CO_2 is bonded with In atom with a bond length of 2.23 Å. The various adsorption configurations of CO_2 on In_2S_3 and $CuInSnS_4$ surfaces are attributed to the coordination environment and charge number of the surface S atoms. The surface S atom of In_2S_3 is an electron-rich site with $[SIn_3]$ coordination structure, while the S atom on $CuInSnS_4$ is an electron-poor center with [SInSnCu] coordination structure (Supplementary Fig. 35 and Table S1). Different adsorption configurations may be the key to determining the direction of electron transfer and thus the selectivity of CO_2 reduction on $CuInSnS_4$ and In_2S_3. Adsorption of CO_2 on the In_2S_3 (0 0 1) crystal plane leads to inconsistent changes in two C=O lengths. The length of the C-O² bond is 1.43 Å, equal to the ordinary C-O (1.43 Å) single bond, while the length of C-O¹ is shortened to 1.19 Å, close to the length of C-O (1.12 Å) in a CO molecule. This asymmetric activation is more likely to cause the rupture of C-O², thereby preferentially producing CO on In_2S_3. In the case of the $CuInSnS_4$ (1 1 1) crystal plane, both C-O bonds are similar in length, measuring 1.26 ± 0.02 Å. They are longer than the C-O bond (1.16 Å) in a free CO_2 molecule, indicating that the bond energy of two C=O bonds of the activated CO_2 is simultaneously weakened. The calculation of the charge density difference reveals the difference in electronic structure and electron flow resulting from the interaction of CO_2 with the surface atoms of In_2S_3 and $CuInSnS_4$. On the In_2S_3 surface, there is extensive charge depletion for the C-O² and S-O² bonds, which implies that these chemical bonds are weakened. In contrast, CO_2 exhibits a wide charge accumulation region on $CuInSnS_4$, leading to the formation of a strong C-S and In-O chemical bond. This strong interaction is beneficial for the firm adsorption of CO_2 on the $CuInSnS_4$ surface, promoting the further deep reduction reaction. The Bader charges analysis further confirms that there is more charge transfer between the $CuInSnS_4$ surface and CO_2 molecules adsorbed on it. The surface of In_2S_3 and $CuInSnS_4$ loses 0.28e and 0.32e, respectively, after CO_2 adsorption (Table S3).

The stable configuration of CO_2 adsorption on $CuInSnS_4$ determines its excellent CO_2 photoreduction activity and selectivity. Therefore, DFT calculations were further carried out to study the conversion pathway of CO_2 on the $CuInSnS_4$ photocatalyst surface, as shown in Fig. 6. In Fig. 6a, the adsorption configuration of $CuInSnS_4$ is shown for each intermediate step, from CO_2 adsorption to CH_4 generation. The C atoms of various intermediates, such as CO_2*, COOH*,
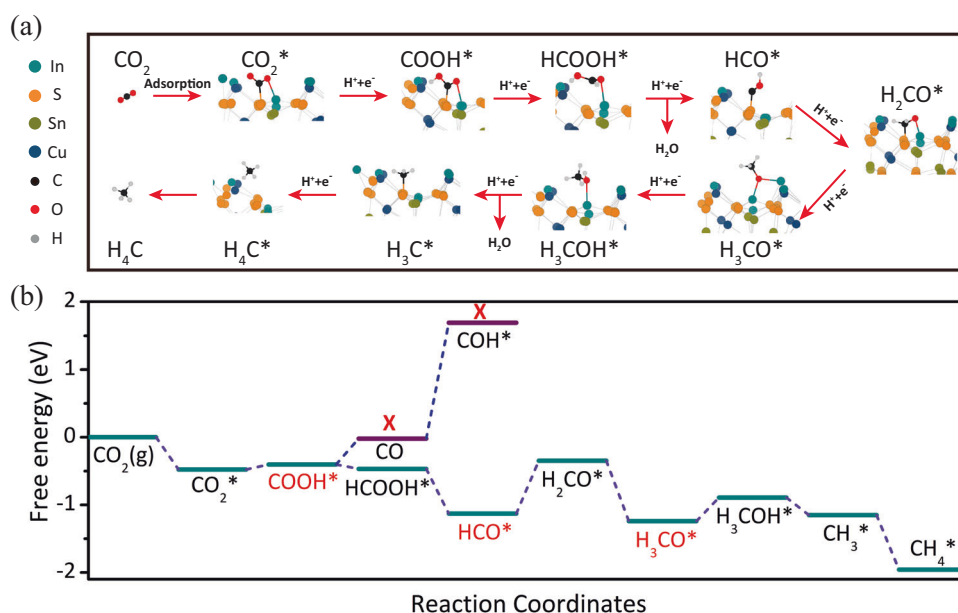

Fig. 6 | DFT calculations of the CO_2 conversion pathway. a Calculated adsorption configuration of CO_2 and reactive intermediates on $CuSnInS_4$. **b** Gibbs free energy diagrams for CO_2 reduction to CH_4 on $CuSnInS_4$.

CHO*, CH_2O*, and CH_3*, remain in a stable bond to the electron-deficient S atoms of the CuInSnS$_4$ nano-single crystal (111) plane. With the addition of protons and electrons, the removal of the H_2O molecule results in the breaking of the chemical bond between O atoms of intermediates and In atoms on CuInSnS$_4$. Moreover, unlike most metal sulfide photocatalysts, the hydrogenation of CO_2 adsorbed on the CuInSnS$_4$ surface to COOH* is an easy step, requiring only a potential energy barrier of 0.075 eV[33], as shown in Fig. 6b. This is attributed to the fact that the electrons are localized on the O^2 atom of CO_2 molecules in the S-C-O-In adsorption configuration of CO_2 on the CuInSnS$_4$ surface to facilitate the addition of protons, thus lowering the formation energy of COOH* intermediates. However, converting COOH* to CO is an endothermic reaction that must overcome an energy barrier of 0.46 eV. On the other hand, the continuous hydrogenation of COOH* intermediates to produce HCOOH* is an exothermic reaction, promoting the hydrogenation of CO_2. The formation of H_2CO* intermediates is the rate-limiting step for further hydrogenation processes, but the hydrogenation of H_2CO* to H_3CO* and finally to CH_4 is thermodynamically spontaneous. Therefore, CuInSnS$_4$ can achieve high selectivity for CH_4 products. Additionally, the adsorption energies of each intermediate product can explain the high CH_4 selectivity. Supplementary Fig. 36 shows that the adsorption energies of CH_4, CH_3OH, and HCOOH on the CuInSnS$_4$ surface are −0.17, −0.61, and −0.67 eV, respectively, with CH_4 having the highest adsorption energy. This indicates that CH_4 products are most easily desorbed from the CuInSnS$_4$ surface, which is one of the reasons why the CuInSnS$_4$ photocatalyst has high selectivity for the photoreduction of CO_2 into CH_4.

The photoreduction mechanism of CO_2 on the CuSnInS$_4$ surface is proposed in Fig. 7. The first step involves CO_2 adsorbing on the catalyst surface to form the unique S-C-O-In structural unit. This process weakens the C=O double bond in the CO_2 molecule while non-metallic S atoms serve as adsorption sites, ensuring a strong bond to the C atom of CO_2. This benefits the continuous reduction of CO_2 molecules into COOH*, HCO*, H_3CO* intermediates, and ultimately into CH_4 on the catalyst surface through the assistance of photogenerated electrons and protons. Lastly, the low adsorption energy of CH_4 on the catalyst surface facilitates its quick release, completing the full photocatalytic cycle reaction.

In summary, a CuSnInS$_4$ nano-single-crystal photocatalyst with exposed (111) facets is successfully prepared by a simple one-step hydrothermal reaction. Under visible-light irradiation, the CuSnInS$_4$ nano-single crystal photocatalyzes the conversion of CO_2 and H_2O into main products of CH_4 with a generation rate of 6.53 μL h^{-1}, significantly higher than that of single metal sulfides (In_2S_3, Cu_2S, and SnS_2). The electron-poor center sulfur atom on the CuSnInS$_4$ (111) crystal plane acts as the site for CO_2 adsorption and activation, which leads to the activation of the two symmetrical C=O double bonds of CO_2 molecule to form a stable S-C-O-In transition state. This induces CH_4 generation via the conversion route of COOH*→HCOOH*→H_2CO*→H_3CO*→CH_4*. However, the asymmetric activation of CO_2 by monometallic sulfides is more likely to result in the cleavage of individual C-O bonds in the CO_2 molecule, leading to the preferential photoreduction of CO_2 to CO. This work provides a distinctive understanding of catalysts for CO_2 adsorption and activation for the CO_2 selective conversion to help the conversion of CO_2 resources into high-value-added products.

Methods

Preparation of CuInSnS$_4$ nanocrystal

A simple one-step hydrothermal method was used to synthesize CuInSnS$_4$ nanocrystal photocatalyst with the cubic crystal structure. The detailed operation process is as follows. Firstly, 1 mmol of CuCl, 1 mmol of SnCl$_4$·5H$_2$O, and 1 mmol of InCl$_3$·4H$_2$O were added to 40 mL of deionized water to form a solution under vigorous stirring. Then, 5 mmol of TAA was dissolved in the above-mixed solution and stirred at room temperature for 30 min. Finally, the resulting mixed solution was transferred to a 50 mL Teflon-lined autoclave and sealed into a stainless steel tank for hydrothermal reaction. The hydrothermal temperature is controlled at 160, 180, and 200 °C for 24 hours. After the reaction, the product was collected and washed with deionized water, and dried under vacuum at 60 °C. The obtained samples were labeled CuInSnS$_4$ (160 °C), CuInSnS$_4$ (180 °C), and CuInSnS$_4$ (200 °C) according to the reaction temperature. The detailed preparation processes of CuInSnS$_4$ modified Pt, CoO, NiO, and Co(OH)$_2$ cocatalysts can be seen in supplementary information.

Characterization

X-ray diffractometer (D8 Advance, Bruker) was used to analyze the crystal structure of the catalyst. The XRD test range is 10°−80°, and the scan rate is 10° min^{-1}. Scanning electron microscopy (su8010, Hitachi) was used to observe the surface morphology of the catalyst. The element composition and ratio of the sample are detected by EDS. The apparent morphology and high-resolution TEM image of the catalyst were tested by transmission electron microscope (TEM, TECNAI G2F20, FEI Company). At the same time, SAED and element mapping images of the catalyst were obtained in the TEM measurement mode. A UV-VIS-NIR Spectrophotometer (Cary 500) was used to obtain the catalyst UV-VIS-NIR DRS, in which BaSO$_4$ was used as a standard sample for 100% light transmission. The Micromeritics 3020 M physical adsorption instrument was used to obtain the nitrogen adsorption and desorption curves of different catalysts. The specific surface area of each catalyst was calculated from the type of nitrogen adsorption and desorption curves. The catalyst and dried potassium bromide were evenly ground, and 20 mg was weighed and pressed into slices, then placed in a quartz infrared tube for a carbon dioxide adsorption infrared test. In situ infrared spectra measurements were performed using a Fourier-transform infrared spectrometer (Nicolet iS50 FT-IR Spectrometer) equipped with a mercury cadmium telluride detector (Supplementary Fig. 37). In situ infrared spectra were recorded by averaging 32 scans at a resolution of 4 cm^{-1}. To initiate the experiment, the catalyst was placed in a 250 mL quartz tube and compacted into a film. The tube was then subjected to vacuum treatment for 60 min. Subsequently, high-purity CO_2 gas was introduced, and the quartz tube was sealed. A liquid sampler was used to inject 60 μL of deionized water into the sealed quartz tube. The tube was heated with a hot blower to vaporize the
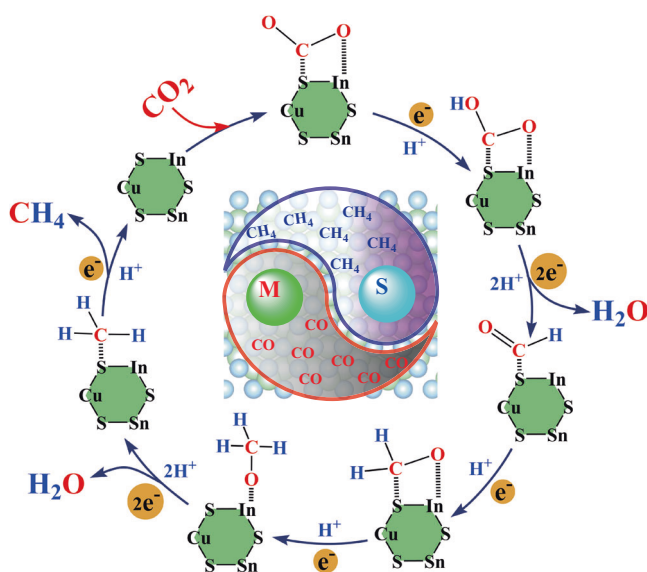

Fig. 7 | CO$_2$ photoreduction pathway. Proposed photocatalytic mechanism for CO_2 reduction on the CuInSnS$_4$. The backgroup crystal structure was created by VESTA program[56].

deionized water. The quartz tube was positioned in the FT-IR spectrometer, ensuring that the incident light of the infrared spectrometer was perpendicular to the sample surface. A xenon lamp visible-light source was introduced to directly illuminate the sample surface. Infrared spectra were recorded after pretreating the catalyst in a vacuum, introducing CO_2 gas, and vaporizing deionized water, respectively. After the introduction of light, infrared spectra were recorded every 5 min. Gas chromatography-mass spectrometry (Agilent 7890B, Agilent 5977B MSD) was used to analyze $^{13}CH_4$ and ^{13}CO. Electron paramagnetic resonance spectroscopic measurements were performed at room temperature using a Bruker A300 EPR spectrometer.

Photocatalytic performance

300 W xenon lamp (Microsolar 300, Beijing Perfectlight Technology Co., Ltd.) was equipped with a 420 nm cutoff wavelength filter as a light source that simulates visible light for photocatalytic CO_2 reduction tests. Firstly, 50 mg of catalyst was dispersed in 5 mL of deionized water and sonicated for 10 min. Then the catalyst was dropped into a watch glass with a diameter of 3 cm and dried at 80 °C. Subsequently, the dried catalyst was placed in a quartz reactor with a volume of ~250 cm^3, and then high-purity CO_2 gas (99.999%) was introduced to replace all the air. The flow rate of carbon dioxide gas was ~100 mL/min and lasted for 1 h. Finally, 50 μL deionized water was injected into the quartz reactor from the rubber stopper through a gas chromatography liquid syringe (maximum range, 50 μL), and the reactor was heated with a hair dryer to evaporate the water into water vapor. As a result, water is present in the form of water vapor throughout the reaction. The reactor was placed under a xenon lamp for photocatalytic reaction, and the current of the xenon lamp was 16 A. After 1 h of illumination, 0.5 mL of gas was extracted from the reactor with a 1 mL gas chromatograph gas syringe and injected into the gas chromatograph for product analysis and detection. Among them, H_2, O_2, and N_2 are detected by a thermal conductivity detector. CH_4 was detected by the flame ionization detector. CO passes through the flame ionization detector after being transformed by the nickel reformer. The product was qualitatively and quantitatively analyzed by gas chromatography retention time and appearance standard curve method.

Theoretical calculations

The density functional theory calculations were performed using the VASP code with the projected augmented wave method[54]. Generalized gradient approximation in the scheme of Perdew-Bueke-Ernzerhof was used for the exchange-correlation functional[54]. The PBEsol exchange-correlation function was adopted in the optimization calculations. Grimme's DFT-D3 scheme was used to describe the long-range vdW interactions[54]. The cutoff energy of the basis function was 420 eV. For the $CuSnInS_4$ (1 1 1) crystal plane, a $2 \times 2 \times 1$ supercell with a four-layer slab was constructed, and only the top two layers were allowed to relax. A vacuum region of 12 Å was set above the surface for periodic boundary conditions, and dipole correction was also applied. Gamma-centered $1 \times 1 \times 1$ grid k-points were used for the interface. Geometry relaxation was performed until the energy, and atomic forces converged to be smaller than 10^{-5} eV and 0.03 eV/Å. Charge transfers were calculated using the Bader charge analysis[54,55].

The free energy of each reaction intermediate was determined by: $G = E + ZPE - TS$. The electronic energy was directly obtained from DFT calculations. The zero-point energy and entropy correction (TS, T = 298.15 K) were computed from vibration analysis according to standard methods. The adsorption-free energy of the adsorbates can be calculated using: $\Delta G_{ads} = \Delta E_{ads} + \Delta ZPE - T\Delta S$, where ΔE_{ads} is the adsorption energy of the adsorbates, and ΔZPE and ΔS are the difference between ZPE and S, respectively. After the adsorption-free energies of the adsorbates are obtained, the reaction-free energies of CO_2 reduction reaction elementary steps can be determined correspondingly by using the computational hydrogen electrode model[40].

Data availability

The authors declare that the data supporting the findings of this study are available in the paper and its supplementary information files. Source data are provided with this paper.

References

1. Zhang, Q. et al. Designing covalent organic frameworks with Co-O$_4$ atomic sites for efficient CO_2 photoreduction. *Nat. Commun.* **14**, 1–11 (2023).
2. Xu, R. et al. Tandem photocatalysis of CO_2 to C_2H_4 via a synergistic rhenium-(I) bipyridine/copper-porphyrinic triazine framework. *J. Am. Chem. Soc.* **145**, 8261–8270 (2023).
3. Shen, Y. et al. Room-temperature photosynthesis of propane from CO_2 with Cu single atoms on vacancy-rich TiO_2. *Nat. Commun.* **14**, 1–9 (2023).
4. Chai, Y. et al. Distortion of the coordination structure and high symmetry of the crystal structure in In_4SnS_8 microflowers for enhancing visible-light photocatalytic CO_2 reduction. *ACS Catal.* **11**, 11029–11039 (2021).
5. Shi, X. et al. Highly selective photocatalytic CO_2 methanation with water vapor on single-atom platinum-decorated defective carbon nitride. *Angew. Chem. Int. Ed.* **61**, e2022030 (2022).
6. Park, H. R., Pawar, A. U., Pal, U., Zhang, T. & Kang, Y. S. Enhanced solar photoreduction of CO_2 to liquid fuel over rGO grafted NiO-CeO_2 heterostructure nanocomposite. *Nano Energy* **79**, 105483 (2021).
7. Kamada, K. et al. Photocatalytic CO_2 reduction using a robust multifunctional iridium complex toward the selective formation of formic acid. *J. Am. Chem. Soc.* **142**, 10261–10266 (2020).
8. Ding, J. et al. Core–shell covalently linked graphitic carbon nitride–melamine–resorcinol–formaldehyde microsphere polymers for efficient photocatalytic CO_2 reduction to methanol. *J. Am. Chem. Soc.* **144**, 9576–9585 (2022).
9. Hao, Y. C. et al. Metal-organic framework membranes with single-atomic centers for photocatalytic CO_2 and O_2 reduction. *Nat. Commun.* **12**, 1–11 (2021).
10. Xia, Y. et al. Highly selective CO_2 capture and its direct photochemical conversion on ordered 2D/1D heterojunctions. *Joule* **3**, 2792–2805 (2019).
11. Zhu, J. et al. Asymmetric triple-atom sites confined in ternary oxideenabling selective CO_2 photothermal reduction to acetate. *J. Am. Chem. Soc.* **143**, 18233–18241 (2021).
12. Liu, Y. et al. Improving CO_2 photoconversion with ionic liquid and Co single atoms. *Nat. Commun.* **14**, 1–11 (2023).
13. Tan, T. H. et al. Unlocking the potential of the formate pathway in the photo-assisted Sabatier reaction. *Nat. Catal.* **3**, 1034–1043 (2022).
14. Yang, S. et al. Microenvironments enabled by covalent organic framework linkages for modulating active metal species in photocatalytic CO_2 Reduction. *Adv. Funct. Mater.* **32**, 2110694 (2022).
15. Nguyen, H. L. & Alzamly, A. Covalent organic frameworks as emerging platforms for CO_2 photoreduction. *ACS Catal.* **11**, 9809–9824 (2021).
16. Guo, R. T., Zhang, Z. R., Xia, C., Li, C. F. & Pan, W. G. Recent progress of cocatalysts loaded on carbon nitride for selective photoreduction of CO_2 to CH_4. *Nanoscale* **15**, 8548–8577 (2023).
17. Zhai, R. et al. A review of phosphorus structures as CO_2 reduction photocatalysts. *Small* **19**, 2207840 (2023).
18. Laghaei, M., Ghasemian, M., Lei, W., Kong, L. & Chao, Q. A review of boron nitride-based photocatalysts for carbon dioxide reduction. *J. Mater. Chem. A* **11**, 11925–11963 (2023).
19. Li, C., Xu, Y., Tu, W., Chen, G. & Xu, R. Metal-free photocatalysts for various applications in energy conversion and environmental purification. *Green. Chem.* **19**, 882–899 (2017).
20. Biswas, S., Dey, A., Rahimi, F. A., Barman, S. & Maji, T. K. Metal-free highly stable and crystalline covalent organic nanosheet

for visible-light-driven selective solar fuel production in aqueous medium. *ACS Catal.* **13**, 5926–5937 (2023).

21. Yuan, Y. P., Cao, S. W., Liao, Y. S., Yin, L. S. & Xue, C. Red phosphor/g-C$_3$N$_4$ heterojunction with enhanced photocatalytic activities for solar fuels production. *Appl. Catal., B* **140-141**, 164–168 (2013).

22. Hu, Z., Lu, Y., Liu, M., Zhang, X. & Cai, J. Crystalline red phosphorus for selective photocatalytic reduction of CO$_2$ into CO. *J. Mater. Chem. A* **9**, 338–348 (2021).

23. Qu, M., Qin, G., Fan, J., Du, A. & Sun, Q. Boron-rich boron nitride nanomaterials as efficient metal-free catalysts for converting CO$_2$ into valuable fuel. *Appl. Surf. Sci.* **555**, 149652 (2021).

24. Wang, Y. et al. Openmouthed β-SiC hollow-sphere with highly photocatalytic activity for reduction of CO$_2$ with H$_2$O. *Appl. Catal., B* **206**, 159–167 (2017).

25. Xu, G. et al. Integrating the g-C$_3$N$_4$ nanosheet with B–H bonding decorated metal–organic framework for CO$_2$ activation and photoreduction. *ACS Nano* **12**, 5333–5340 (2018).

26. Cao, Y. et al. B–O bonds in ultrathin boron nitride nanosheets to promote photocatalytic carbon dioxide conversion. *ACS Appl. Mater. Interfaces* **12**, 9935–9943 (2020).

27. Chen, P. et al. Rare-earth single-atom La–N charge-transfer bridge on carbon nitride for highly efficient and selective photocatalytic CO$_2$ reduction. *ACS Nano* **14**, 15841–15852 (2020).

28. Feng, H. et al. Surface nonpolarizationof g-C$_3$N$_4$ by decoration with sensitized quantum dots for improved CO$_2$ photoreduction. *ChemSusChem* **11**, 4256–4261 (2018).

29. Zhang, Y., Xia, B., Ran, J., Davey, K. & Qiao, S. Z. Atomic-level reactive sites for semiconductor-based photocatalytic CO$_2$ reduction. *Adv. Energy Mater.* **10**, 1903879 (2020).

30. Cao, Y. et al. Modulating electron density of vacancy site by single Au atom for effective CO$_2$ photoreduction. *Nat. Commun.* **12**, 1675 (2021).

31. He, Y. et al. 3D hierarchical ZnIn$_2$S$_4$ nanosheets with rich Zn vacancies boosting photocatalytic CO$_2$ reduction. *Adv. Funct. Mater.* **29**, 1905153 (2019).

32. Wang, J. et al. Effect of S vacancy in Cu$_3$SnS$_4$ on high selectivity and activity of photocatalytic CO$_2$ reduction. *Appl. Catal., B* **297**, 120498 (2021).

33. Li, X. et al. Selective visible-light-driven photocatalytic CO$_2$ reduction to CH$_4$ mediated by atomically thin CuIn$_5$S$_8$ layers. *Nat. Energy* **4**, 690–699 (2019).

34. Zhu, X. et al. Unique dual-sites boosting overall CO$_2$ photoconversion by hierarchical electron harvesters. *Small* **17**, 2103796 (2021).

35. Bae, K. L., Kim, J., Lim, C. K., Nam, K. M. & Song, H. Colloidal zinc oxide-copper(I) oxide nanocatalysts for selective aqueous photocatalytic carbon dioxide conversion into methane. *Nat. Commun.* **8**, 1156 (2017).

36. Deng, Y. et al. Synergy effect between facet and zero-valent copper for selectivity photocatalytic methane formation from CO$_2$. *ACS Catal.* **12**, 4526–4533 (2022).

37. Horani, F. & Lifshitz, E. Unraveling the growth mechanism forming stable γ-In$_2$S$_3$ and β-In$_2$S$_3$ colloidal nanoplatelets. *Chem. Mater.* **31**, 1784–1793 (2019).

38. Rangappa, A. P. et al. In situ growth of Ag$_2$S quantum dots on SnS$_2$ nanosheets with enhanced charge separation efficiency and CO$_2$ reduction performance. *J. Mater. Chem. A* **10**, 7291–7299 (2022).

39. Liu, Y., Liu, M. & Swihart, M. T. Reversible crystal phase interconversion between covellite CuS and high chalcocite Cu$_2$S nanocrystals. *Chem. Mater.* **29**, 4783–4791 (2017).

40. Zhang, Y. et al. Photocatalytic CO$_2$ reduction: identification and elimination of false-positive results. *ACS Energy Lett.* **7**, 1611–1617 (2022).

41. Weng, B., Qi, M. Y., Han, C., Tang, Z. R. & Xu, Y. J. Photocorrosion inhibition of semiconductor-based photocatalysts: basic principle, current development, and future perspective. *ACS Catal.* **9**, 4642–4687 (2019).

42. Yu, H., Huang, X., Wang, P. & Yu, J. Enhanced photoinduced stability and photocatalytic activity of CdS by dual amorphous cocatalysts: synergistic effect of Ti(IV)-hole cocatalyst and Ni(II)-electron cocatalyst. *J. Phys. Chem. C.* **120**, 3722–3730 (2016).

43. Netzsch, P., Pielnhofer, F. & Höppe, H. A. From S–O–S to B–O–S to B–O–B bridges: Ba[B(S$_2$O$_7$)$_2$]$_2$ as a model system for the structural diversity in borosulfate chemistry. *Inorg. Chem.* **59**, 15180–15188 (2020).

44. Xiong, X. et al. Photocatalytic CO$_2$ reduction to CO over Ni single atoms supported on defect-rich zirconia. *Adv. Energy Mater.* **10**, 2002928 (2020).

45. Wang, Y. et al. Direct and indirect Z-scheme heterostructure-coupled photosystem enabling cooperation of CO$_2$ reduction and H$_2$O oxidation. *Nat. Commun.* **11**, 3043 (2020).

46. He, Y. et al. Quantitative evaluation of carrier dynamics in full-spectrum responsive metallic ZnIn$_2$S$_4$ with indium vacancies for boosting photocatalytic CO$_2$ reduction. *Nano Lett.* **22**, 4970–4978 (2022).

47. Caminiti, R., D'Ilario, L., Martinelli, A., Piozzi, A. & Sadun, C. DSC, FT-IR, and energy dispersive X-ray diffraction applied to the study of the glass transition of poly(p-phenylene sulfide). *Macromolecules* **30**, 7970–7976 (1997).

48. Yu, X. et al. Lithium storage in conductive sulfur-containing polymers. *J. Electroanal. Chem.* **573**, 121–128 (2004).

49. Wang, X. et al. Sulfurized polyacrylonitrile cathodes with high compatibility in both ether and carbonate electrolytes for ultrastable lithium–sulfur batteries. *Adv. Funct. Mater.* **29**, 19029029 (2019).

50. Xu, C. et al. Photothermal coupling factor achieving CO$_2$ reduction based on palladium-nanoparticle-loaded TiO$_2$. *ACS Catal.* **8**, 6582–6583 (2018).

51. Xu, J. et al. Efficient infrared-light-driven CO$_2$ reduction over ultrathin metallic Ni-doped CoS$_2$ nanosheets. *Angew. Chem. Int. Ed.* **60**, 8705–8709 (2021).

52. Jiao, X. et al. Partially oxidized SnS$_2$ atomic layers achieving efficient visible-light-driven CO$_2$ reduction. *J. Am. Chem. Soc.* **139**, 18044–18051 (2017).

53. Li, J. et al. Interfacial engineering of Bi$_{19}$Br$_3$S$_{27}$ nanowires promotes metallic photocatalytic CO$_2$ reduction activity under near-infrared light irradiation. *J. Am. Chem. Soc.* **143**, 6551–6559 (2021).

54. Tang, W., Sanville, E. & Henkelman, G. A grid-based Bader analysis algorithm without lattice bias. *J. Phys. Condens. Mat.* **21**, 084204 (2009).

55. Sanville, E., Kenny, S. D., Smith, R. & Henkelman, G. Improved grid-based algorithm for bader charge allocation. *J. Comput. Chem.* **28**, 899–980 (2007).

56. Momma, K. & Izumi, F. *VESTA 3* for three-dimensional visualization of crystal, volumetric and morphology data. *J. Appl. Crystallogr.* **44**, 1272–1276 (2011).

Acknowledgements

Author contributions

X.W. and Z.Z. conceived the concept and supervised the research. Y.K., W.L., and J.S. performed the DFT calculations. Y.C. and M.L. performed the experimental work. J.L., R.Y., and W.D. helped to write—review & edit the manuscript. All authors designed the experiments, analyzed the data, and drafted the manuscript.

Competing interests

The authors declare no competing interests.

Additional information

Supplementary information The online version contains supplementary material available at https://doi.org/10.1038/s41467-023-41943-x.

Correspondence and requests for materials should be addressed to Zizhong Zhang.

Peer review information *Nature Communications* thanks Tao Yu and the other, anonymous, reviewer(s) for their contribution to the peer review of this work. A peer review file is available.

Reprints and permissions information is available at http://www.nature.com/reprints

Publisher's note Springer Nature remains neutral with regard to jurisdictional claims in published maps and institutional affiliations.